

## Electric Field Responsive Smart Fluids from Olive Pulp Powder

Özlem Erol\*

Chemistry Department, Science Faculty, Gazi University, 06560, Ankara, TÜRKİYE

<https://orcid.org/0000-0003-2156-537X>

\*corresponding author: [erol@gazi.edu.tr](mailto:erol@gazi.edu.tr)

(Received: 12.03.2024, Accepted: 12.08.2024, Published: 25.11.2024)

**Abstract:** This study aims to evaluate one of the wastes of the olive oil industry, olive pulp powder (OP), due to its consisting of mainly polarizable lignocellulosic biomass, as a dispersed phase in electric field-responsive (ER) fluid whose rheological properties can be tuned by an externally applied electric field ( $E$ ). The supplied OP was extracted with  $n$ -hexane, and structural and thermal analysis revealed the removal of residual oil and soluble small molecules. The OP and  $n$ -hexane treated-OP (h-OP) were dispersed in silicon oil (SO), and their rheological and dielectric properties, and dispersion stabilities were investigated. According to the flow test results, the yield stresses ( $\tau_y$ ) of both dispersions increased with increasing concentration and the  $E$ . The  $\tau_y$  of the OP/SO and h-OP/SO dispersions (25 wt%) under  $E=3.5$  kV/mm increased 29 and 130 times greater than their  $\tau_y$  values under no  $E$ , respectively. The dielectric spectrum analysis showed that enhanced interfacial polarization and decreased nonpolarized forces after the  $n$ -hexane extraction improved the ER response of the h-OP/SO dispersion. The enhanced dispersion stability (90%) was determined for h-OP/SO dispersion at 25 wt%. As a result, the h-OP could be a sustainable candidate for evaluation as a dispersing phase of ER fluids for vibration-damping systems.

**Key words:** Sustainability, Agricultural industry waste, Olive pulp powder, Electric field responsive fluids, Upcycling

### 1. Introduction

With the advancement of technology, the rise in productivity of agricultural products leads to significant increases in waste production. Due to the high amount of waste generated in the agricultural industry, its high cost and environmental effects lead to a substantial problem. Both academic and industrial studies on transforming bio-based products obtained from raw biomass and renewable agricultural resources into eco-friendly products capable of rivaling petroleum-based alternatives in the market have recently attracted attention [1]. The significant rise in the world population leads to a rapid increase in food consumption and, therefore, to a rise in agricultural industry-related wastes released. For this reason, it is essential to encourage producers and consumers to reduce solid waste production by recycling, reusing, and upcycling. Recently, increasing awareness of environmentally friendly products and choosing biodegradable materials have come to the fore to overcome and reduce environmental problems.

Smart materials with rheological characteristics that can be manipulated using an external electric field ( $E$ ) are promising for applications such as hydraulic control systems, robotic systems, the automotive industry, microfluidics, and drug release [2] and one of them is called electric-field responsive or electrorheological (ER) fluids. The suitable particles that can be polarized by the  $E$  effect are dispersed in an insulating carrier fluid like silicone

oil (SO) to obtain an ER fluid. In the ER fluid, fibrillar or columnar-like structures perpendicular to the electrodes are formed by aligning the dispersed particles in the applied  $E$  direction. These reversibly formed structures allow the dispersion to transform from a liquid-like state to a solid-like state. Many ER-active materials have been developed and reported in the literature to date. The first studies were mostly on materials such as silica, alumina, zeolite, cellulose, and starch, which derive their polarizability from the water adsorbed into their structure. Subsequently, interest has turned to intrinsically polarizable materials, such as various conductive polymers, carbon nanotubes, graphene oxide, and poly(ionic) liquids, whose polarizability does not depend on the water in their structure [3].

Considering sustainability and green chemistry principles, priority should be given to studies on developing ecological products in ER fluids or using green strategies to prepare ER active materials. In this respect, because of their biodegradability and natural abundance, the use of biologically sourced materials such as cellulose [4], chitin, chitosan [5, 6, 7], porous chitosan [7], starch [8, 9, 10], alginate [11], etc., and their modified forms or composites have been reported as ER active materials. In addition to environmentally friendly materials, there have been limited studies in the literature on using agricultural wastes as ER active materials. In a study, the ER performance of microcrystalline cellulose obtained from rice husk waste by applying alkaline, bleaching, and hydrolysis processes were examined, and its electric field response was reported to be lower compared to previously prepared microcrystalline cellulose using different sources but exhibited viscoelastic properties with similar trends [12]. In another study, microcrystalline cellulose obtained from rice husk waste was used to prepare phosphatized microcrystalline cellulose via the esterification reaction of cellulose in the presence of urea and phosphoric acid, and its dispersions in SO displayed a higher ER response [13]. Also, waste rice husk was utilized to prepare nano-silica particles by applying acid and heat treatments, and it was reported that its dispersion in SO responded strongly to the  $E$  [14]. In another study, the dispersion of organic waste spent coffee grounds obtained after extracting coffee from roasting coffee grounds (containing trace metals and hemicellulose, cellulose, lignin, and some residual acids released during roasting of coffee) in SO was reported to show higher ER activity at a particular threshold concentration value (40% by volume) than pre-waste state ground coffee dispersion in SO [15]. It was suggested that the ER activity of spent coffee grounds was due to some functional groups remaining on the grain surfaces after the extraction process.

In the olive oil production process, olive pulp (OP) is obtained by processing the residual solid waste, mostly consisting of seeds, shell, and pulp, remaining after the extraction of crude olive oil [16]. High amounts of organic matter, fat, carbohydrates, proteins, and water-soluble phenolic species remained in the OP, and its composition mainly consists of lignocellulosic biomass (30-41.6% lignin, 35.3-49.0% cellulose, pectic polymers, hemicelluloses, oils, and minerals) [16]. The utilization of agro-industrial residue, OP, is increasingly gaining attention and becoming more commonplace as a fuel, an additive in animal feed, and a filler in polymer composites [17]. Since this agricultural industry waste comprises polarizable structures such as cellulose, hemicellulose, and lignin, OP can be evaluated as a dispersed phase in electric field-responsive smart fluids.

This study aimed to evaluate one of the agro-industrial wastes, the OP, as an electric field-responsive material. The supplied OP particles were washed with  $n$ -hexane using a Soxhlet apparatus to remove residual oil and soluble small fatty acid molecules. After ball-milling, OP and  $n$ -hexane treated OP (h-OP) were used as the dispersed phase for preparing ER fluid. OP and h-OP dispersions were prepared in SO. Their dielectric

properties and dispersion stabilities were investigated, and their rheological properties under  $E$  were explored via steady shear, oscillatory shear, and creep-recovery tests.

## 2. Materials and Methods

### 2.1. Materials

Olive pulp (OP) particles, approximately 150  $\mu\text{m}$  size were kindly supplied under the brand name MOROVA by the Şenol Food Industry Incorporated Company (Aydın, Türkiye). The supplied OP particles comprised the pulp-rich part obtained by processing the solid waste pulp remaining after the oil was taken from the olive fruit after drying and granulating. The extraction solvent, *n*-hexane, was purchased from Merck and used as received. Silicone oil (SO, polydimethylsiloxane with viscosity of 1.0 Pa s and density of 0.967 g/mL) was provided from Sigma Aldrich and vacuum dried before preparing ER fluids as a dispersing medium.

### 2.2. Preparation of ER fluids

Before using the OP particles for the preparation of ER fluids as a dispersing phase and for further characterization studies, the residual oil, soluble small molecules, and fatty acids were extracted via the Soxhlet extraction at 100°C using *n*-hexane for 24 h. After vacuum drying at 60°C for 24 h, to obtain fine-grade powder form for further uses, the OP particles and *n*-hexane extracted OP particles (h-OP) were grounded using a ball-miller at 20 Hz for 20 min (Retsch, MM400, Germany). The ER dispersions were prepared by dispersing OP and h-OP at mass percent concentration series of 5-25 wt% in SO with 5% increments. The dispersions were mixed mechanically and then thoroughly using a probe sonicator (Sonics, Vibracell, USA) to make uniform dispersion, and utilized for the rheological, dielectric, and dispersion stability measurements.

### 2.3. Characterization methods

The primary functional groups present in OP and h-OP were determined via attenuated total reflectance Fourier transform infrared spectroscopy (ATR-FTIR, Thermo Scientific, Nicolet IS50, USA), operating with a resolution of 4  $\text{cm}^{-1}$  and conducting 64 scans. Elemental analysis of the samples was conducted using Thermo Scientific Flash 2000 organic elemental analyzer (USA). The thermal analysis of the samples was conducted using a Hitachi STA 7300 (Japan) thermogravimetric analyzer device in the range of an ambient temperature to 800°C under an inert Ar atmosphere, and the heating rate was adjusted to 10°C/min. The degradation temperature at which the most significant mass loss occurred ( $T_{\text{max}}$ ) was measured from the maximum value of the mass loss derivative. After coating with a thin layer of gold using a sputter coater (Leica EM ACE200, Germany), the morphologies of the samples were investigated via scanning electron microscopy (SEM) with an accelerating voltage of 5 kV (SEM, Hitachi SU5000, Japan). The four-probe technique was employed to measure the electrical conductivities of the OP and h-OP by using their compressed disc-shaped pellets with defined dimensions at 25°C (Entek Electronic, FPP 470-A, Türkiye), and the average electrical conductivity values of the samples were derived by collecting measurements from at least five distinct locations on the pellet. The apparent densities of OP and h-OP were determined using the calculated volume and measured mass of the prepared pellets as mentioned earlier.

### 2.4. Dielectric measurements

An impedance analyzer (Agilent E4980A precision LCR meter, Japan) equipped with a parallel plate capacitor for liquids (Agilent 16452A, Japan) was used to measure the

dielectric characteristics of the OP and h-OP dispersions within the frequency range from 20 Hz to 1 MHz.

### **2.5. Dispersion stability measurements**

The dispersion stabilities of the OP and h-OP dispersions were determined by taking the percentage ratios of the height of the dispersion occupied by the particle-rich part to the entire height of the dispersion.

### **2.6. The rheological measurements**

The rheological measurements of all the OP and h-OP dispersions were conducted at 25°C using a torque rheometer (Thermo-Haake RS600, Germany) connected to the DC electric field generator (HCL 14, FuG Elektronik, Germany). During measurements, the gap between the measuring geometries of 35.0 mm parallel plates was adjusted to 1.0 mm. After pre-shearing ( $60 \text{ s}^{-1}$ ) for 60 s, the dispersions were allowed to reach equilibrium without shearing for 60 s under a particular  $E$  application before initiating each measurement. The flow curves were generated by measuring shear stresses ( $\tau$ ) and viscosities ( $\eta$ ) as a function of shear rates ( $\dot{\gamma}$ ) under various  $E$  values. The elastic and loss moduli were determined via dynamic oscillatory rheological measurements to display the viscoelastic properties of the ER fluids. Firstly, elastic, and viscous modulus values of the dispersions were measured as a function of shear stress at a constant frequency of 1 Hz as a function of the  $E$  to determine the linear viscoelastic regions (LVER). The LVER was determined by observing the limit of the plateau region of elastic modulus ( $G'$ ) versus the stress curve after where the  $G'$  became stress-dependent. Secondly, the viscoelastic moduli were measured over a 1-100 Hz frequency range at constant stress levels within the predefined LVER at various  $E$  values. The creep-recovery tests were conducted through measurement of the strain values over a specified period of 100 s during the application of the applied stress ( $\tau > 0$ ) instantaneously and recovered strain values after releasing the applied stress ( $\tau = 0$ ) for another 100 s.

## **3. Results**

### **3.1. Characterizations**

The OP and h-OP samples displayed the specific FTIR spectrum of a lignocellulosic compound dominantly (Figure 1). Both materials exhibited similar peaks without any significant peak shifts but with a decrease in peak intensity for several peaks, as discussed below. The OP presented a broad band with a maximum of around  $3300 \text{ cm}^{-1}$ , assigned to the stretching vibration of the O–H involved in hydrogen bonding. The two peaks around  $2922$  and  $2852 \text{ cm}^{-1}$ , identified as the asymmetric and symmetric C–H stretching vibrations in methyl and methylene groups found in cellulose, lignin, hemicellulose, and fatty acids, were notably observed in OP [18, 19].

The peaks observed at various wavenumbers corresponded to specific molecular vibrations are given as following: The band observed at  $1740 \text{ cm}^{-1}$  was assigned to the stretching vibration of C=O bonds in carbonyl, carboxyl, and acetyl groups;  $1635 \text{ cm}^{-1}$  represented a composite signal encompassing bands associated with conjugated C–O bonds in quinones coupled with C=O stretching in various groups, as well as contributions from adsorbed water molecules and C=C stretching in the aromatic skeleton of lignin; C=O stretching vibrations in the amide bond of residual proteins;  $1514 \text{ cm}^{-1}$  indicated the stretching vibration of C=C bonds in the aromatic skeleton of lignin and N-H bending and C-N stretching vibrations in the residual proteins; the signals at  $1455$  and  $1416 \text{ cm}^{-1}$  were linked to the deformation of C–H bonds in lignin and carbohydrates;  $1373 \text{ cm}^{-1}$

corresponded to the bending vibration of C–H bonds in cellulose and hemicellulose, along with the stretching vibration of C–O bonds in the guaiacyl unit of lignin;  $1232\text{ cm}^{-1}$  represented the stretching vibration of C–H bonds in the syringyl unit of lignin and C–N stretching vibrations found in residual proteins;  $1030\text{ cm}^{-1}$  was designated as representing the skeletal vibration of the C–O–C pyranose ring in cellulose [19, 20] and  $\sim 600\text{--}750\text{ cm}^{-1}$  may be corresponded to the stretching of the C–S bonds in the residual sulfur containing amino acids [22]. All peaks were retained for h-OP after Soxhlet extraction of OP with *n*-hexane. However, the reductions of the broad peak spanning from  $3600$  and  $3000\text{ cm}^{-1}$ , the peaks around  $2922$  and  $2852\text{ cm}^{-1}$ , and the peak at  $1740\text{ cm}^{-1}$  can be ascribed to the successful removal of the excess oil, fatty acids, and non-polar soluble molecules in the OP after Soxhlet extraction for h-OP.

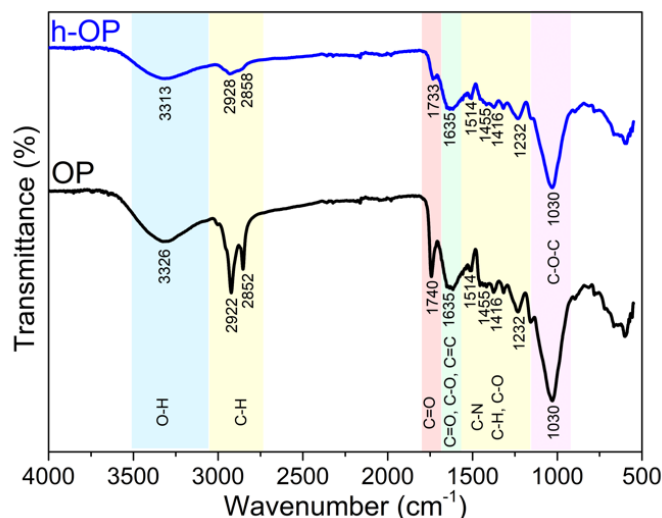


**Figure 1.** ATR-FTIR spectra of the OP and h-OP

The elemental composition of the OP depends on the origin of the compound [21]. As a lignocellulosic material, the main substances in OP are carbon sources constituting hemicellulose, cellulose, and lignin. Additionally, protein and extractives as nitrogen, sulfur sources, and fat are other constituents of the OP [22]. The removal of the excess olive oil, fatty acids, and soluble extractive molecules was also revealed by elemental analysis. According to the elemental analysis results, the decrease in C and H content of the OP after Soxhlet extraction revealed the successful removal of excess olive oil, fatty acids, and small soluble non-polar molecules. On the other hand, *n*-hexane extraction could not effectively remove the most polar compounds, including proteins and amino acids (which were sources of N and S). The elemental analysis results were in good agreement with the ATR-FTIR results.

**Table 1.** The % composition obtained from elemental analysis (N, C, H, S) of the OP and h-OP

Sample	N (%)	C (%)	H (%)	S (%)
OP	1.8343±0.0335	51.0651±0.071	6.4708±0.0247	0.1409±0.0077
h-OP	3.9993±0.2572	48.2369±0.037	5.8969±0.2877	0.1572±0.0079

A comparison of the thermogravimetry (TG)/differential TG (DTG) curves of the OP and h-OP is presented in Figure 2a-b. The OP and h-OP exhibited two main decomposition steps in an inert atmosphere during the thermal degradation (Figure 2a). A slight mass loss of 6% and 5% occurred between  $40^{\circ}\text{C}$  and  $130^{\circ}\text{C}$ , corresponding to the evaporation of moisture adsorbed to the OP and the h-OP, respectively. The second decomposition step occurred within the  $150\text{--}550^{\circ}\text{C}$  temperature range for both samples. According to the previous studies, the primary constituents of the OP, i.e. hemicellulose, cellulose, and

lignin, showed consecutive pyrolysis steps involving primary pyrolysis of hemicellulose occurred between 150-315°C giving a shoulder at lower temperatures, and cellulose occurred between 300-400°C with a well-defined sharp peak followed by mainly lignin pyrolysis occurred over a broad temperature span from 100°C to 900°C as a wide shoulder on the main degradation domain [23, 24]. Besides, the decomposition temperature intervals of these components can partially overlap [19]. The OP studied in this work showed a  $T_{\max}$  at 320°C followed by decay with a long tail and a shoulder around 366°C which disappeared for h-OP (Figure 2b) due to the removal of remaining olive oil [25] in the OP after the Soxhlet extraction process, corresponding to approximately 4% mass loss difference, which was consistent with the elemental analysis results by considering the difference in C and H content between OP and h-OP. Hemicellulose, composed of various saccharides, has random and amorphous structures and, thus, has weaker thermal stability than cellulose, with an ordered and long unbranched linear polymeric structure consisting of glucose units with a glycosidic bond. For that reason, the shoulder is usually observed for hemicellulose content of the OP at lower temperatures of the main decomposition peak. However, this shoulder did not appear in the DTG curve of the OP and h-OP due to the superposition of its decomposition with cellulose and lignin [19]. Additional broad peaks with insignificant intensity observed above 600°C were detected, likely indicating the decomposition of mineral matter in the samples [26].

The SEM images in Figure 2c-d indicated that both samples demonstrated approximately the same size, irregular, particulate-like, and slightly porous structures with cavities on the surfaces. In previous studies, spherical-like with a low aspect ratio and porous structures were reported for olive pulp powder [24, 27].

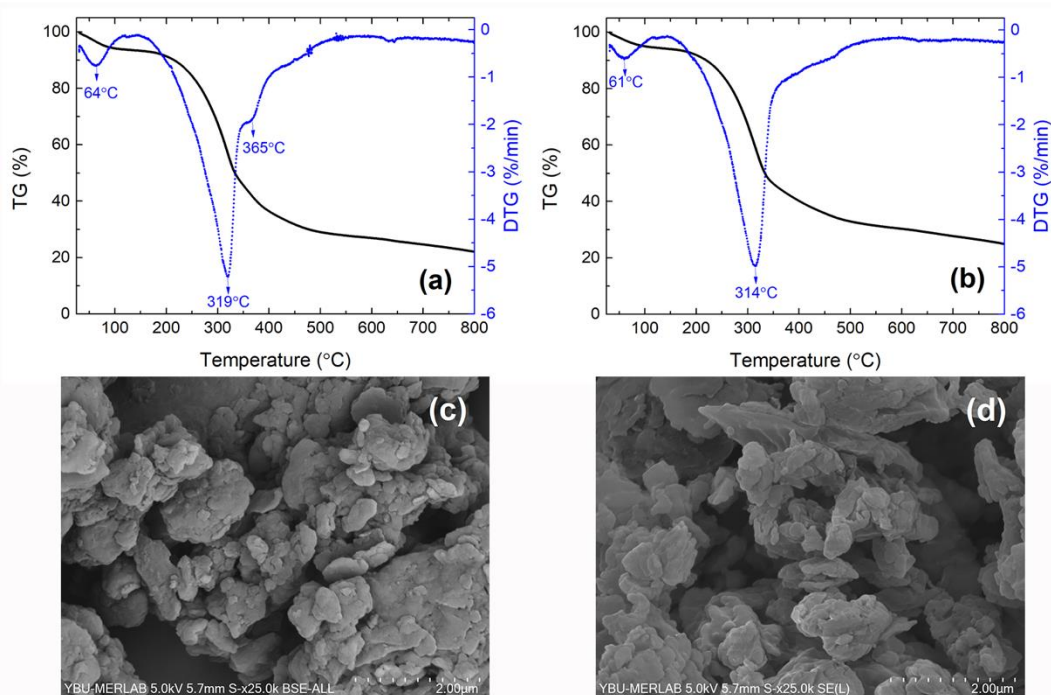


**Figure 2.** TG/DTG curves of (a) OP and (b) h-OP, and SEM image of (c) OP and (d) h-OP

Various critical key factors affect the electric field response of the ER fluid including particle size distribution, shape, wettability, electrical conductivity, dielectric characteristics of the particles, the concentration of the dispersion, the  $E$ , temperature, properties of carrier fluid, and dispersion stability [2]. Therefore, developing ER fluids with the desired high performance is challenging given the complexity of these variables. The conductivity of the dispersed particles is recommended to be in the semiconducting range of  $10^{-6}$ – $10^{-12}$  S/cm [28]. The conductivities of OP and h-OP were measured as

$(8.05 \pm 0.83) \times 10^{-7}$  S/cm and  $(5.44 \pm 1.00) \times 10^{-7}$  S/cm, respectively, indicating their being in the desired range as an ER active material. Additionally, Soxhlet extracting with n-hexane may lead to a relative decrease in the conductivity of OP due to the removal of the fatty acid molecules.

### 3.2. Dielectric properties

The strength of the electric field response of an ER fluid has a strong relationship with its dielectric properties, and thus, so does the polarizability of the dispersed particles. A good ER response requires larger interfacial polarizability and dielectric loss peaks in the  $10^2$  to  $10^6$  Hz range. The dielectric analysis was conducted to explore the correlation between the intensity of the ER phenomenon and the dielectric characteristics of ER fluids. The spectra of dielectric permittivity ( $\epsilon'$ ) and loss ( $\epsilon''$ ) of the OP/SO and h-OP/SO dispersions are shown in Figure 3 for 25 wt%.

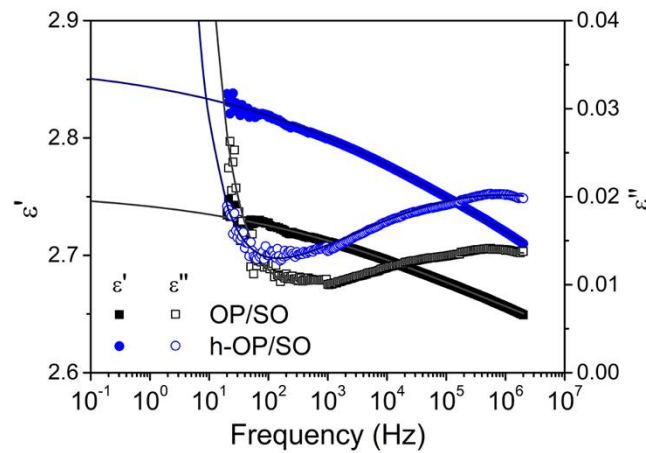


**Figure 3.** Dielectric spectra of the OP/SO and h-OP/SO dispersions (25 wt%). The solid lines show the fitted the  $\epsilon'$  and  $\epsilon''$  spectra using the Equation 1

The Havriliak–Negami (HN) dielectric relaxation equation (Equation 1), combined with the conductivity term, was applied to fit the experimental complex dielectric permittivity,  $\epsilon^*(\omega)$  [29, 30]. The first two terms indicate the HN function for a single relaxation process, and the last term corresponds to the contribution of conductivity to the dielectric loss spectrum in Equation 1 [31]. Additionally, the  $\omega$  is the angular frequency ( $f$ ), where  $\omega = 2\pi f$ . The  $\tau_{HN}$  is the average relaxation time of the polarization process and is equal to  $1/2\pi f_{max}$  where  $f_{max}$  represents the frequency at which the dielectric loss peak occurs. The  $\Delta\epsilon$  is the dielectric relaxation strength, which displays the difference in the  $\epsilon'$  at low frequency ( $\epsilon_s$ ) with the  $\epsilon'$  at the high-frequency limit,  $\epsilon(\infty)$ . The exponents  $\alpha$  and  $\beta$  related to the broadness and asymmetry of the respective relaxation loss peak, respectively ( $0 \leq \alpha, \beta \leq 1$ ), and describe the distribution of the relaxation times. The  $\sigma$  is the conductivity of the dispersion,  $\epsilon(0)$  is the vacuum permittivity ( $8.854 \times 10^{-12}$  F/m), and the  $N$  denotes the exponent that defines the conduction process. The relevant dielectric parameters obtained are tabulated in Table 2.

$$\epsilon^*(\omega) = \epsilon'(\omega) - i\epsilon''(\omega) = \epsilon(\infty) + \frac{\Delta\epsilon}{[1 + (i\omega\tau_{HN})^{1-\alpha}]^\beta} - i\left(\frac{\sigma}{\epsilon_0\omega}\right)^N \quad (1)$$

**Table 2.** Dielectric parameters obtained from the fitted dielectric spectra according to the Equation 1 for the OP/SO and h-OP/SO dispersions (25 wt%)

Sample	$\epsilon_s$	$\epsilon(\infty)$	$\Delta\epsilon = \epsilon_s - \epsilon(\infty)$	$f_{max}$ (Hz)	$\tau_{HN}$ (s)	$\alpha$	$\beta$	$\sigma$
OP/SO	2.755	2.556	0.199	$1.0 \times 10^5$	$1.6 \times 10^{-6}$	0.196	0.72	$1.8 \times 10^{-11}$
h-OP/SO	2.866	2.578	0.288	$8.0 \times 10^5$	$2.0 \times 10^{-7}$	0.178	0.99	$1.1 \times 10^{-11}$

The  $\Delta\epsilon$  relates to the degree of interfacial polarization, whereas the relaxation time  $\tau_{HN}$  denotes the rate of polarization. Maximizing the strength of the relaxation process is crucial for achieving a high ER response [31]. Although the  $\Delta\epsilon$  values were relatively low, both dispersions exhibited the required polarization response to the  $E$  at the desired rate of  $10^2$ – $10^6$  Hz range. The h-OP/SO exhibited a relatively higher magnitude of interfacial polarization and shorter relaxation time than OP/SO, consistent with the ER performance discussed in section 3.4. At lower frequencies, the dispersions exhibited pronounced electrode polarization traits attributed to the abundant polar hydroxyl groups in cellulose [32]. Comparable rises in dielectric loss were reported in low-frequency regions for nanocellulose and microcellulose particles dispersed in olive oil, attributed to the connection of the cellulose particles in the large agglomerates leading to the conductivity through the dielectric oil medium [31]. The observed difference in dielectric properties of OP/SO and h-OP/SO can be associated with an increase in interphase boundaries after removing the excess fatty acids and extractive molecules, which may ease the polarizability of the particles.

### 3.3. Dispersion stabilities

The dispersion stability is one of the essential criteria to assess the long-term usage of ER fluids and possible industrial applications. The dispersion stability is desired to be maintained during application, and ER activity is weakened drastically if there is a sedimentation tendency of the dispersed phase. The nature, morphology, size, and surface properties of the dispersed particles, type, and viscosity of the medium, the presence of any stabilizer such as surfactants, and density mismatch between the dispersed phase and carrier fluid are the main factors affecting the dispersion stability. Numerous attempts have been undertaken in the literature to enhance the dispersion stability [33]. The apparent densities of the dispersed particles were determined to evaluate the effect of the density on the dispersion stability. The apparent density of the OP and h-OP were determined as  $1.197 \pm 0.002$  g/cm<sup>3</sup> and  $1.235 \pm 0.010$  g/cm<sup>3</sup>, respectively. The density of carrier fluid, SO, is known as 0.970 g/cm<sup>3</sup>. The relatively slight density contrast between the dispersed OP and h-OP and the SO may lead to improved dispersion stability.

The OP/SO and h-OP/SO dispersions with various concentrations were allowed to settle undisturbed for one month. Their dispersion stabilities were assessed by measuring the change in anti-sedimentation ratio with time at 25°C. Initially, all the dispersions were in a well-dispersed state (Figure 4). Throughout the settling process, dispersed particles in the fluid gradually settled to the bottom of the container, leaving a relatively clearer carrier fluid above the sediment enriched with particles. Over time, the anti-sedimentation ratio reached an equilibrium value faster at lower and slower at higher concentrations for both samples.

The anti-sedimentation ratios of the dispersions enhanced as the dispersion concentration rose, attributed to the heightened interactions between the dispersed phase and dispersing medium, along with the increase in dispersion viscosity [34]. On the other hand, the effect of gravitational forces on dispersed particles became prominent at lower concentrations, resulting in lower dispersion stability. When the results of SEM analysis and density measurement were evaluated, it was concluded that both samples had similar particle size, morphology, and density values. Thus, the anti-sedimentation ratio improvement from 74 % to 90 % reached at the end of 30 days for 25 wt% was attributed to the improved interfacial adhesion between the carrier fluid and h-OP after Soxhlet extraction by *n*-hexane of OP.

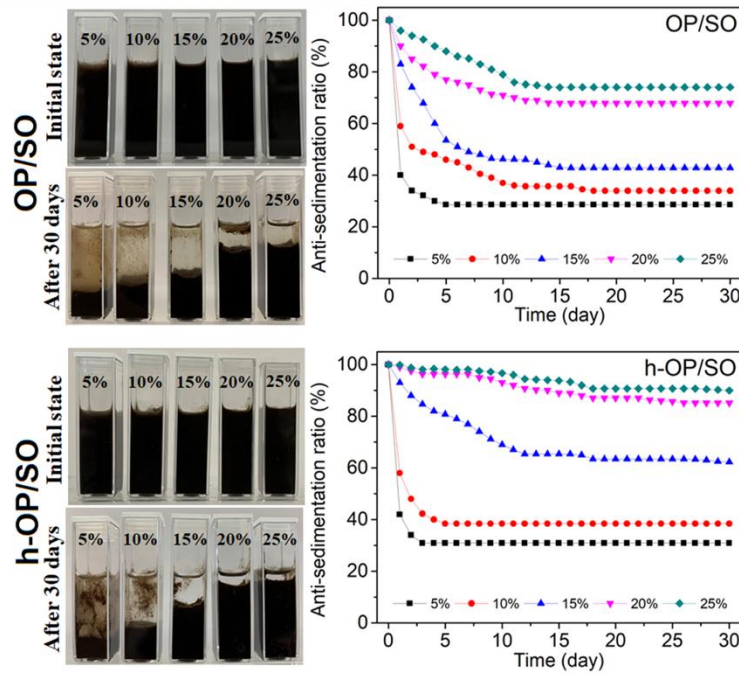


**Figure 4.** The visual appearance of the OP/SO and h-OP/SO dispersions at the initial of the dispersion stability test and after 30 days of observation for 5–25 wt%, and the change in the anti-sedimentation ratio with time for the OP/SO and h-OP/SO dispersions

### 3.4. Electrorheological properties

#### 3.4.1. The flow behavior

The steady shear rheological measurements were carried out under appropriate controllable  $E$  values to understand the behavior of dispersions to the  $E$ . Various rheological models, including Bingham [35], de Kee–Turcotte [36], Herschel–Bulkley [37], Cho–Choi–Jhon (CCJ) [38], or Seo–Seo [39] can be utilized to depict the rheological characteristics of the ER fluids. In this study, the CCJ model (Equation 2) was selected to demonstrate the flow behavior of both dispersions over the shear range examined since the successful fitting curves of shear stress were observed for both dispersions studied. The flow behavior of both ER dispersions across a broad spectrum of shear rates was examined using the CCJ model, and the best-fitting curves (solid curves) are depicted in Figure 5 for 25 wt% concentration.

$$\tau = \frac{\tau_y}{(1 + (t_1\dot{\gamma})^\alpha)} + \eta_\infty \left(1 + \frac{1}{(t_2\dot{\gamma})^\beta}\right)\dot{\gamma} \quad (2)$$

The CCJ model equation comprises six parameters where  $\tau$  is the shear stress,  $\tau_y$  is the dynamic yield stress,  $\eta_\infty$  is the viscosity at a high shear rate,  $\dot{\gamma}$  is the shear rate,  $t_1$  and  $t_2$  are time constants, and the exponent  $\alpha$  is associated with the reduction of shear stress while the exponent  $\beta$  has the range of  $0 < \beta \leq 1$  [38]. When subjected to an  $E$ , randomly distributed particles were drawn towards each other and linked due to the electric field polarization effect, resulting in the formation of chain/columnar-like structures. In the low shear rate region, the shear stress increased rapidly, and the mechanical shear force was insufficient to break the linking force between electric field-induced particles forming fibrillar or columnar-like structures. Thus, the curve maintained high shear stress at low shear rate values. The shear stress and viscosity values were raised with the increase of the  $E$  for both dispersions.

The rates at which fibrillar-like structures, formed through induced electrostatic interactions, are broken down and rebuilt between the dispersed particles under shear force are mainly dependent on the race between electrostatic forces arising from interfacial polarization of dispersed particles and hydrodynamic forces resulting from shear flow within the dispersion [40, 41]. At low  $\dot{\gamma}$ , electrostatic forces prevailed, while at high  $\dot{\gamma}$ , hydrodynamic forces disrupted aligned structures and facilitated flow. The electrical-induced structures were then completely broken down, and the shear stress values raised gradually with rising  $\dot{\gamma}$ , showing Newtonian fluid behavior beyond the critical  $\dot{\gamma}$  because there was not enough time for the chain-like structure to reform adequately during swift shear deformation. These changes in the microstructure of dispersed particles led to a significant decrease in viscosity, displaying a shear-thinning behavior. At low  $E$  range (0.5–1.5 kV/mm), the breakage of the aligned dispersed particles was not substantial, and a wide plateau emerged in the shear stress until reaching the critical  $\dot{\gamma}$ . As the  $E$  increased to a higher range, the flow curve displayed a decline in shear stress at a moderate  $\dot{\gamma}$  values, range due to the apparent destruction rate against the reformation rate of the fibrillar-like structures [39]. Similar behaviors were observed for the dispersions of porous chitosan particles in carrier fluid olive oil [42].

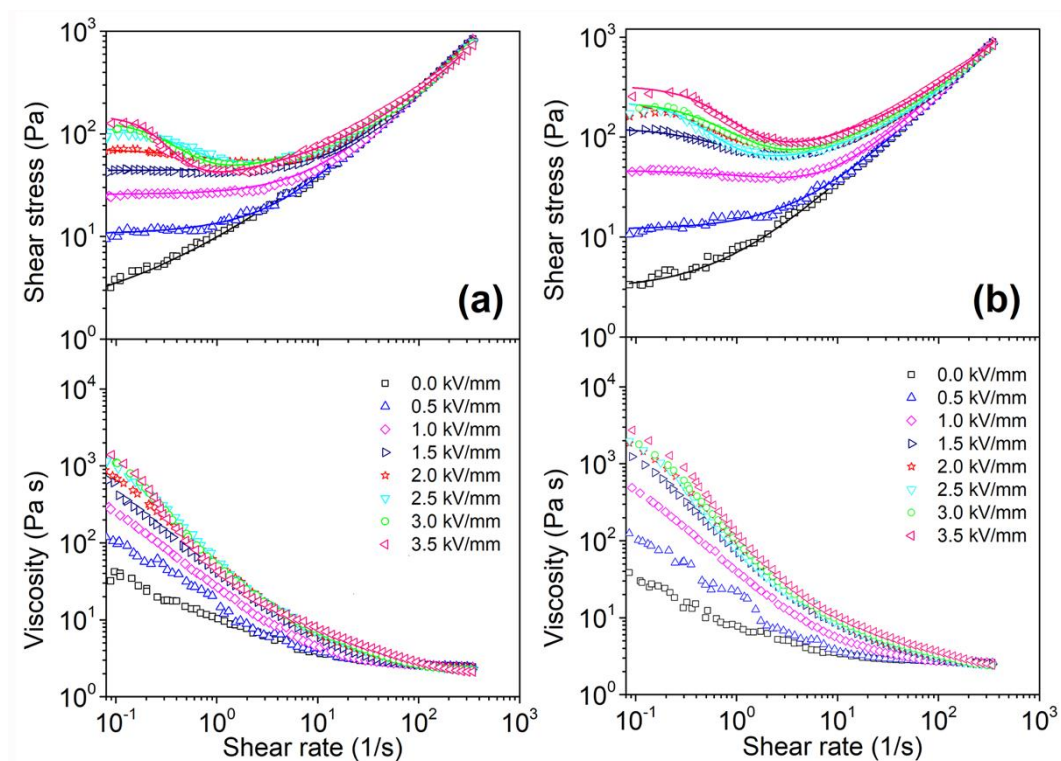


**Figure 5.** The change in shear stress and viscosity (flow curves) of (a) OP/SO and (b) h-OP/SO dispersions under various  $E$  for 25 wt% concentration. The solid curves in the shear stress-shear rate graph shows the best-fitted curves using the Equation 2

The flow curves were obtained for the OP/SO and h-OP/SO dispersions with a series of concentrations between 5-25 wt% to explore how the particle concentration influences the ER performance and to determine the optimum concentration value for further rheological measurements. Therefore, the  $\tau_y$  values of the dispersions determined according to the Equation 2 were compared. The dependence of the  $\tau_y$  on the  $E$  as a function of OP and h-OP particle mass percentages are shown in Figure 6a and Figure 6b, respectively. The  $\tau_y$  was increased with increasing particle mass percentage and the  $E$ . With increasing  $E$ , the shear resistance related to the yield stress was strengthened due to the increased electrostatic forces between the particles arranged in the direction of  $E$ . This observation was more pronounced as the particle concentration increased due to the decrease in interparticle distance and the increase in the number of denser

fibrillar/columnar-like structures [43]. On the other hand, the  $\tau_y$  values displayed two distinct linear trends on the log-log scale with the  $E$ , intercepting at  $E=2.0$  kV/mm for all dispersions (the dotted lines in Figure 6). After that point, the slope was changed, and the increase in the  $\tau_y$  with the  $E$  was observed to be insignificant. This observation could be attributed to the saturation of the interfacial polarization above this electric field strength [44].

The power law equation describes the correlation between  $\tau_y$  and  $E$  as  $\tau_y \propto E^\alpha$ , where  $\alpha$  serves as the index parameter indicating the slope of the fitted curve on a log-log scale used to evaluate the mechanism of the ER effect. In the case of  $\alpha$  is equal to 2 and 1.5, the ER mechanism corresponds to the polarization model and the conduction model, respectively [45]. However, the dispersed particle size and shape, surface characteristics and concentration, as well as the dielectric properties of the dispersion on the  $\tau_y$  affect this relationship in certain instances [43]. The slope of the  $\tau_y$  curve was approached from 0.5 to 1.5 and 0.7 to 2.0 as the dispersion mass percentage was increased from 5% to 25% for OP/SO and h-OP/SO dispersion for up to 2 kV/mm, respectively. With increasing the dispersed particle concentration, the behavior approached the conduction and polarization model for the OP/SO and h-OP/SO dispersion, respectively. Therefore, the response of OP particles dispersed in SO under an  $E$  indicated that it was primarily influenced by the significant impact of the conductivity mismatch between the particles and the carrier medium [46]. A similar index parameter value of  $<1.5$  was previously reported for various biomaterial-based ER fluids, including  $\alpha$ -chitin nanorods [47], porous chitosan [7], phosphorylated potato starch [9], and polypyrrole–silica–methylcellulose composite [48]. The decrease in the index  $\alpha$  value ( $<1.5$ ) was attributed the formation of the non-polarization forces such as hydrogen bonding interactions of the dispersed particles with the carrier fluid and surface polarization saturation [43, 47, 49]. In another study, poly(ionic liquid) based ER fluid whose ER response originated from local ion motion tended to follow the conduction model, whereas its composite with polyaniline led to incline to polarization model [50]. On the other hand, h-OP/SO dispersion was consistent with the polarization model, whose  $\alpha$  value was 2.0, indicating that the removal of fatty acids and extractives contributes to the enhancement of polarization of OP particles by decreasing the non-polarization forces. In a study, nanocellulose particles dispersed in castor oil containing ricinoleic acid were reported to exhibit the index parameter approaching 1.5 with increasing concentration, due to the hindering of the electrostatic forces because of H-bonding or van der Waals interactions between the hydroxyl groups in the nanocellulose particles and the carrier fluid castor oil [44].

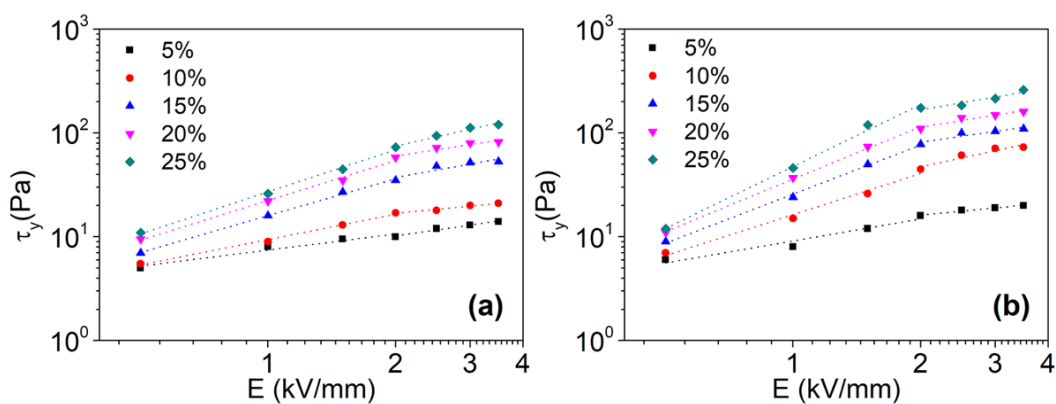


**Figure 6.** The yield stress as a function of the  $E$  for (a) OP/SO and (b) h-OP/SO dispersions for concentrations between 5 to 25 wt%, the dotted lines show the trendlines of a power-law scaling

### 3.4.2. Oscillation rheology results

The viscoelastic characteristics of the OP/SO and h-OP/SO dispersions (25 wt%) were examined by the dynamic oscillation experiments. The shear stress sweep test was conducted firstly to determine the LVER of the dispersions at a constant frequency of 1 Hz, as shown in Figure 7a. The elastic modulus ( $G'$ ) values were independent of the applied shear stress in the LVER and increased with the  $E$ . Furthermore, the enhanced polarization forces between the particles led to a shift of the LVER to higher shear stresses with increasing  $E$ . At the end of the plateau region, the electrical-induced fibrillar structures became broken, and the  $G'$  values began to decrease by the applied oscillatory shear deformation. The  $G'$  was increased by around 12 and 35 times for OP/SO and h-OP/SO dispersions, respectively, under 3.0 kV/mm in the LVER compared to off-field conditions, indicating h-OP/SO dispersion showed significantly greater elastic dominant character than OP/SO dispersion.

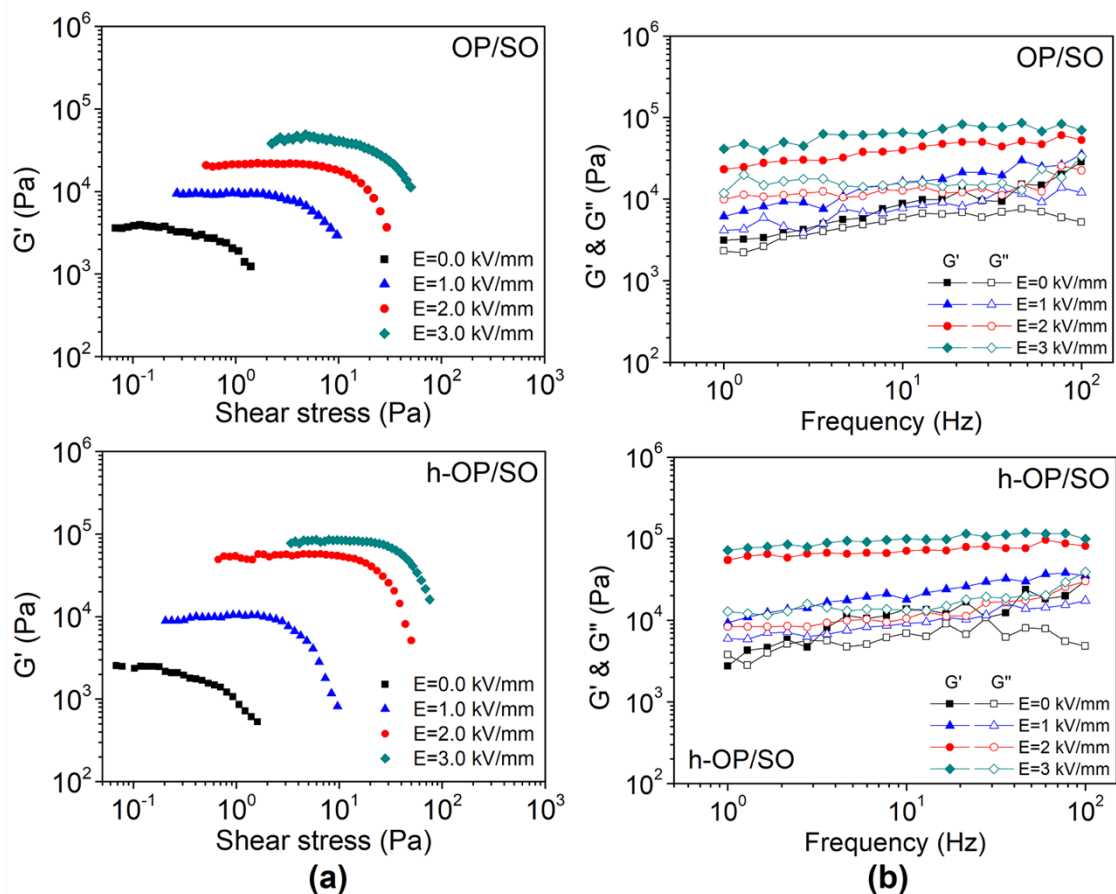


**Figure 7.** (a) The shear stress dependence of  $G'$  and (b) the frequency dependence of the  $G'$  and  $G''$  for OP/SO and h-OP/SO dispersions

Secondly, the change in  $G'$  and viscous modulus ( $G''$ ) values of both dispersions were determined as a function of the frequency in the range of 1–100 Hz at constant stress values in the previously determined LVER at various  $E$  values, as shown in Figure 7b. In the off-field, the  $G'$  slightly exceeded the  $G''$  within the studied frequency range and both moduli values increased with frequency for both dispersions. Thus, the OP/SO and h-OP/SO dispersions behaved like weak gel and confirmed the presence of the low yield stress values at 25 wt% concentrations obtained from the steady shear flow curve tests. The main reason for such gel-like formation without the  $E$  could be attributed to the percolation network formation and the structural organization of the dispersed particles due to the restricted motions through dominant attraction forces between them. The formation of similar percolation networks for various particles such as clay [51],

detonation nanodiamond [52], and porous chitosan particles [7] were reported, and the reasons were attributed to the particle anisotropy.

With the  $E$ , the  $G'$  values dramatically exceeded the  $G''$  and reached about 65 kPa and 100 kPa at the electric field of 3 kV/mm for OP/SO and h-OP/SO, respectively, demonstrating that the predominant behavior was solid-like, characterized by a stable plateau region, rather than viscous. The  $G'$  values of h-OP/SO dispersion were 1.5 times greater than that of OP/SO dispersion under  $E$ , indicating the enhanced polarization ability and higher solidification of h-OP dispersion. The moduli values were increasing with  $E$ , indicating that the electrical-induced fibrillar structures of the OP/SO and h-OP/SO dispersions were not broken in the studied frequency range, and the elastic and solid-like properties of the dispersions were strengthened with  $E$ . The increased gap between the values of  $G'$  and  $G''$  with increasing the  $E$  demonstrated the increase in the elastic component of the dispersions.

### 3.4.3. Creep and recovery results

In a creep recovery test, the deformation behavior of a material is evaluated by initially measuring the strain under a constant shear stress load, followed by unloading, over a specified duration at a constant temperature. After the stress is removed, there is only a partial recovery that is controlled by the retardation and the corresponding creep for viscoelastic materials, and the recovery ratio ( $\chi$ ) was defined to evaluate the contribution of the elastic character of the ER fluid and calculated using the following Equation 3 [53]:

$$\chi = \frac{\gamma_i - \gamma_f}{\gamma_i} \quad (3)$$

where  $\gamma_i$  denotes the achieved strain prior to the removal of the applied shear stress ( $\tau_0$ ), while  $\gamma_f$  represents the strain following the removal of the  $\tau_0$ . A creep-recovery test was conducted to monitor the deformation and recovery of the electrically induced structures over time, and the recorded strain as a function of time under various  $E$  for the optimum dispersion, h-OP/SO, is presented in Figure 8.

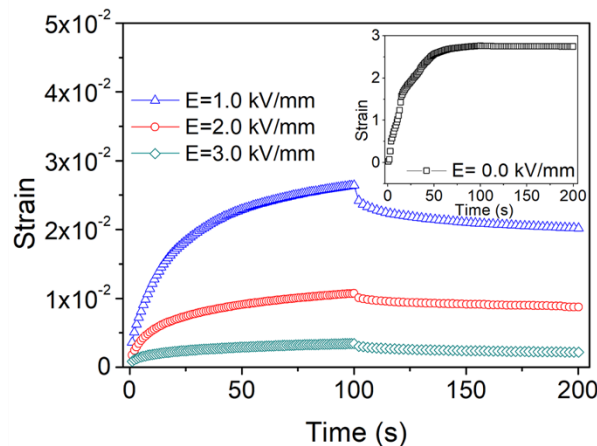


**Figure 8.** Changes in strain over time at different levels of  $E$  during the creep-recovery test for h-OP/SO. The creep-recovery curve of h-OP/SO for off-field is displayed in the inset figure ( $\tau_0 = 5$  Pa for the first 100 s and then  $\tau_0 = 0$  Pa, 25 wt%).

Upon stress loading, an instantaneous strain appeared and subsequently escalated over time, reaching a maximum value indicating time-dependent nonlinear deformation under constant stress. After the removal of the stress loading, subsequent time-dependent reformations were observed under  $E$ . In contrast, almost no recovery was observed

without the presence of the  $E$ , as shown in the inset figure in Figure 8. The strain values obtained during the creep-recovery test decreased as  $E$  increased, suggesting the formation of a more robust solid-like structure with increasing  $E$  [33]. For the h-OP/SO dispersion, the recovery ratios with increasing  $E$  were observed to enhance as following:  $\chi_{E=1\text{kV/mm}}=0.27 < \chi_{E=2\text{kV/mm}}=0.42 < \chi_{E=3\text{kV/mm}}=0.48$ , suggesting increased elastic response among particles at higher  $E$ .

#### 4. Conclusion

By considering environmental issues, the utilization of nontoxic and eco-friendly products as a component of ER fluids is highly desired. With this respect, the agricultural organic waste, the olive pulp (OP), discarded after the olive oil extraction process consisting of sustainable biomass sources, was upcycled as an electric field-responsive smart fluid. The OP was further subjected to Soxhlet extraction by  $n$ -hexane to remove excess residual fatty acids and small molecules that existed in the raw OP. Structural, thermal, morphological, and electrical characterizations of the OP and  $n$ -hexane treated OP (h-OP) samples were performed. Successful removal of the excess oil, fatty acid, and residual small molecules in the OP was revealed by ATR-FTIR, elemental analysis, and TG/DTG analysis. The conductivities of the OP and h-OP were determined to be in the desired semiconducting range for the ER fluids, and relatively lower conductivity was obtained for h-OP compared to OP. Also, the h-OP dispersion showed a relatively higher magnitude of interfacial polarization and shorter relaxation time than that of the OP dispersion due to the improved polarization resulting from the increase in interphase boundaries after the Soxhlet extraction process and decreased nonpolarized forces. The enhanced dispersion stability was determined for h-OP dispersion. Both control shear rate flow curve and oscillation rheological analysis results under the  $E$  indicated that Soxhlet extraction led the OP to display stronger electric field response and higher ER activity. This study suggests that OP, an agricultural industrial waste that occurs in high amounts in the olive oil production process, is a good candidate for upcycling in the field of electric field responsive smart fluids due to its higher dispersion stability and ER activity after being subjected to the pre-washing process by  $n$ -hexane.

---

#### *Authorship contribution statement*

**Ö. Erol:** Conceptualization, Methodology, Investigation, Data Curation, Visualization, Original Draft Writing, Review and Editing.

#### *Declaration of competing interest*

The author declares that she has no known competing financial interests or personal relationships that could have appeared to influence the work reported in this paper.

#### *Acknowledgment*

The author expresses her gratitude to Prof. Dr. H.İ. Ünal (Gazi University, Science Faculty, Chemistry Department) for giving the opportunity to provide the laboratory facility for rheological and electrical studies.

#### *Ethics Committee Approval and/or Informed Consent Information*

As the author of this study, I declare that I do not have any ethics committee approval and/or informed consent statement.

## References

- [1] F. P. La Mantia, M. Morreale, "Green composites: A brief review", *Composites Part A: Applied Science and Manufacturing*, 42(6), 579-588, 2011.
- [2] N. M. Kuznetsov, V. V. Kovaleva, S. I. Belousov, S. N. Chvalun, "Electrorheological fluids: From historical retrospective to recent trends", *Materials Today Chemistry*, 26,101066, 2022.
- [3] K. Zhang, H. J. Choi, "Smart polymer/carbon nanotube nanocomposites and their electrorheological response", *Materials*, 7(5), 3399-3414, 2014.
- [4] V. I. Kordonsky, E. V. Korobko, T. G. Lazareva, "Electrorheological polymer-based suspensions", *Journal of Rheology*, 35(7), 1427-1439, 1991.
- [5] Y. G. Ko, S. S. Shin, U. S. Choi, Y. S. Park, J. W. Woo, "Gelation of chitin and chitosan dispersed suspensions under electric field: Effect of degree of deacetylation", *ACS Applied Materials & Interfaces*, 3(4), 1289-1298, 2011.
- [6] Y. G. Ko, H. J. Lee, S. S. Shin, U. S. Choi, "Dipolar-molecule complexed chitosan carboxylate, phosphate, and sulphate dispersed electrorheological suspensions", *Soft Matter*, 8(23), 6273-6279, 2012.
- [7] N. M. Kuznetsov, Y. D. Zagoskin, A. Y. Vdovichenko, A. V. Bakirov, R. A. Kamyshinsky, A. P. Istomina, T. E. Grigoriev, S. N. Chvalun, "Enhanced electrorheological activity of porous chitosan particles", *Carbohydrate Polymers*, 256, 117530, 2021.
- [8] K. Negita, H. Itou, T. Yakou, "Electrorheological effect in suspension composed of starch powder and silicone oil", *Journal of Colloid and Interface Science*, 209(1), 251-254, 1999.
- [9] J. H. Sung, D. P. Park, B. J. Park, H. J. Choi, M. S. Jhon, "Phosphorylation of potato starch and its electrorheological suspension", *Biomacromolecules*, 6(4), 2182-2188, 2005.
- [10] M. Yavuz, T. Tilki, C. Karabacak, O. Erol, H. I. Unal, M. Uluturk, M. Cabuk, "Electrorheological behavior of biodegradable modified corn starch/corn oil suspensions", *Carbohydrate Polymers*, 79(2), 318-324, 2010.
- [11] Y. G. Ko, H. J. Lee, Y. J. Chun, U. S. Choi, K. P. Yoo, "Positive and negative electrorheological response of alginate salts dispersed suspensions under electric field", *ACS Applied Materials & Interfaces*, 5(3), 1122-1130, 2013.
- [12] B. Sim, D. H. Bae, H. J. Choi, K. Choi, M. S. Islam, N. Kao, "Fabrication and stimuli response of rice husk-based microcrystalline cellulose particle suspension under electric fields", *Cellulose*, 23(1), 185-197, 2016.
- [13] D. H. Bae, H. J. Choi, K. Choi, J. D. Nam, M. S. Islam, N. Kao, "Fabrication of phosphate microcrystalline rice husk based cellulose particles and their electrorheological response", *Carbohydrate Polymers*, 165, 247-254, 2017.
- [14] S. H. Kwon, I. H. Park, C. M. Vu, H. J. Choi, "Fabrication and electro-responsive electrorheological characteristics of rice husk-based nanosilica suspension", *Journal of the Taiwan Institute of Chemical Engineers*, 95, 432-437, 2019.
- [15] Y. Chun, Y. G. Ko, T. Do, Y. Jung, S. W. Kim, U. Su Choi, "Spent coffee grounds: Massively supplied carbohydrate polymer applicable to electrorheology", *Colloids and Surfaces A: Physicochemical and Engineering Aspects*, 562, 392-401, 2019.
- [16] P. Otero, P. Garcia-Oliveira, M. Carpena, M. Barral-Martinez, F. Chamorro, J. Echave, P. Garcia-Perez, H. Cao, J. Xiao, J. Simal-Gandara, M. A. Prieto, "Applications of by-products from the olive oil processing: Revalorization strategies based on target molecules and green extraction technologies", *Trends in Food Science & Technology*, 116, 1084-1104, 2021.
- [17] G. Espadas-Aldana, P. Guaygua-Amaguaña, C. Vialle, J.-P. Belaud, P. Evon, C. Sablayrolles, "Life cycle assessment of olive pomace as a reinforcement in polypropylene and polyethylene biocomposite materials: A new perspective for the valorization of this agricultural by-product", *Coatings*, 11(5), 525, 2021.
- [18] M. Volpe, D. Wüst, F. Merzari, M. Lucian, G. Andreottola, A. Kruse, L. Fiori, "One stage olive mill waste streams valorisation via hydrothermal carbonisation", *Waste Management*, 80, 224-234, 2018.
- [19] S. Sismanoglu, U. Tayfun, C.-M. Popescu, Y. Kanbur, "Effective use of olive pulp as biomass additive for eco-grade TPU-based composites using functional surface modifiers", *Biomass Conversion and Biorefinery*, 13, 12303-12318, 2023.
- [20] M. J. Pancholi, A. Khristi, K. M. Athira, D. Bagchi, "Comparative analysis of lignocellulose agricultural waste and pre-treatment conditions with FTIR and machine learning modeling", *BioEnergy Research*, 16(1), 123-137, 2023.
- [21] H. M. Boundzanga, B. Cagnon, M. Roulet, S. de Persis, C. Vautrin-UI, S. Bonnamy, "Contributions of hemicellulose, cellulose, and lignin to the mass and the porous characteristics of activated carbons produced from biomass residues by phosphoric acid activation", *Biomass Conversion and Biorefinery*, 12(8), 3081-3096, 2022.
- [22] A. I. Martín García, A. Moumen, D. R. Yáñez Ruiz, E. Molina Alcaide, "Chemical composition and nutrients availability for goats and sheep of two-stage olive cake and olive leaves", *Animal Feed Science and Technology*, 107(1), 61-74, 2003.

- [23] V. Benavente, A. Fullana, "Torrefaction of olive mill waste", *Biomass and Bioenergy*, 73, 186-194, 2015.
- [24] S. Lammi, A. Barakat, C. Mayer-Laigle, D. Djenane, N. Gontard, H. Angellier-Coussy, "Dry fractionation of olive pomace as a sustainable process to produce fillers for biocomposites", *Powder Technology*, 326, 44-53, 2018.
- [25] R. Font, M. D. Rey, "Kinetics of olive oil pyrolysis", *Journal of Analytical and Applied Pyrolysis*, 103, 181-188, 2013.
- [26] M. Wzorek, R. Junga, E. Yilmaz, B. Bozhenko, "Thermal decomposition of olive-mill byproducts: A tg-ftir approach", *Energies*, 14(14), 4123, 2021.
- [27] T. Akar, I. Tosun, Z. Kaynak, E. Ozkara, O. Yeni, E. N. Sahin, S. T. Akar, "An attractive agro-industrial by-product in environmental cleanup: Dye biosorption potential of untreated olive pomace", *Journal of Hazardous Materials*, 166(2), 1217-1225, 2009.
- [28] Y. Z. Dong, H. M. Kim, H. J. Choi, "Conducting polymer-based electro-responsive smart suspensions", *Chemical Papers*, 75(10), 5009-5034, 2021.
- [29] J. K. Jung, Y. I. Moon, G. H. Kim, N. H. Tak, "Characterization of dielectric relaxation process by impedance spectroscopy for polymers: Nitrile butadiene rubber and ethylene propylene diene monomer", *Journal of Spectroscopy*, 2020, 8815492, 2020.
- [30] S. Havriliak, S. Negami, "A complex plane analysis of  $\alpha$ -dispersions in some polymer systems", *Journal of Polymer Science Part C: Polymer Symposia*, 14(1), 99-117, 1966.
- [31] N. M. Kuznetsov, V. V. Kovaleva, A. Y. Vdovichenko, S. N. Chvalun, "Natural electrorheological fluids based on cellulose particles in olive oil: The filler size effect", *Colloid Journal*, 85(3), 408-417, 2023.
- [32] M. Hasanin, A. M. Labeeb, "Dielectric properties of nicotinic acid/methyl cellulose composite via "green" method for anti-static charge applications", *Materials Science and Engineering: B*, 263, 114797, 2021.
- [33] O. Erol, H. I. Unal, "Core/shell-structured, covalently bonded TiO<sub>2</sub>/poly(3,4-ethylenedioxythiophene) dispersions and their electrorheological response: The effect of anisotropy", *RSC Advances*, 5(125), 103159-103171, 2015.
- [34] G. T. Ngatu, N. M. Wereley, J. O. Karli, R. C. Bell, "Dimorphic magnetorheological fluids: Exploiting partial substitution of microspheres by nanowires", *Smart Materials and Structures*, 17(4), 045022, 2008.
- [35] E. C. Bingham, *Fluidity and Plasticity*, New York, McGraw-Hill Book Company, Inc., 440 pages, 1922.
- [36] D. D. Ké, G. Turcotte, "Viscosity of biomaterials", *Chemical Engineering Communications*, 6(4-5), 273-282, 1980.
- [37] W. H. Herschel, R. Bulkley, "Konsistenzmessungen von gummi-benzollösungen", *Kolloid-Zeitschrift*, 39(4), 291-300, 1926.
- [38] M. S. Cho, H. J. Choi, M. S. Jhon, "Shear stress analysis of a semiconducting polymer based electrorheological fluid system", *Polymer*, 46(25), 11484-11488, 2005.
- [39] Y. P. Seo, Y. Seo, "Modeling and analysis of electrorheological suspensions in shear flow", *Langmuir*, 28(6), 3077-3084, 2012.
- [40] L. I. Linzhi, G. A. O. Shujuan, "Polyaniline (PANI) and BaTiO<sub>3</sub> composite nanotube with high suspension performance in electrorheological fluid", *Materials Today Communications*, 24, 100993, 2020.
- [41] J.-Y. Hong, M. Choi, C. Kim, J. Jang, "Geometrical study of electrorheological activity with shape-controlled titania-coated silica nanomaterials", *Journal of Colloid and Interface Science*, 347(2), 177-182, 2010.
- [42] N. M. Kuznetsov, Y. D. Zagoskin, A. V. Bakirov, A. Y. Vdovichenko, S. N. Malakhov, A. P. Istomina, S. N. Chvalun, "Is chitosan the promising candidate for filler in nature-friendly electrorheological fluids?", *ACS Sustainable Chemistry & Engineering*, 9(10), 3802-3810, 2021.
- [43] S. Y. Oh, T. J. Kang, "Electrorheological response of inorganic-coated multi-wall carbon nanotubes with core-shell nanostructure", *Soft Matter*, 10(21), 3726-3737, 2014.
- [44] M. A. Delgado-Canto, S. D. Fernández-Silva, C. Roman, M. García-Morales, "On the electro-active control of nanocellulose-based functional biolubricants", *ACS Applied Materials & Interfaces*, 12(41), 46490-46500, 2020.
- [45] B. Zhang, Y. Chen, H. Zheng, C. Li, L. Ma, H. Zhang, B. Wang, C. Hao, "Composites of co-doped graphitic C<sub>3</sub>N<sub>4</sub> nanosheets and TiO<sub>2</sub> nanoparticles for electrorheological fluid applications", *ACS Applied Nano Materials*, 5(1), 1003-1015, 2022.
- [46] J. Liu, X. Wen, Z. Liu, Y. Tan, S. Yang, P. Zhang, "Electrorheological performances of poly(o-toluidine) and p-toluenesulfonic acid doped poly(o-toluidine) suspensions", *Colloid and Polymer Science*, 293(5), 1391-1400, 2015.

- [47] V. V. Kovaleva, N. M. Kuznetsov, A. P. Istomina, O. I. Bogdanova, A. Y. Vdovichenko, D. R. Streltsov, S. N. Malakhov, R. A. Kamyshinsky, S. N. Chvalun, "Low-filled suspensions of  $\alpha$ -chitin nanorods for electrorheological applications", *Carbohydrate Polymers*, 277, 118792, 2022.
- [48] D. J. Yoon, Y. D. Kim, "Synthesis and electrorheological behavior of sterically stabilized polypyrrole-silica-methylcellulose nanocomposite suspension", *Journal of Colloid and Interface Science*, 303(2), 573-578, 2006.
- [49] X. Huang, W. Wen, S. Yang, P. Sheng, "Mechanisms of the giant electrorheological effect", *Solid State Communications*, 139(11), 581-588, 2006.
- [50] C. Zheng, Q. Lei, J. Zhao, X. Zhao, J. Yin, "The effect of dielectric polarization rate difference of filler and matrix on the electrorheological responses of poly(ionic liquid)/polyaniline composite particles", *Polymers*, 12(3), 703, 2020.
- [51] R. K. Pujala, H. B. Bohidar, "Slow dynamics and equilibrium gelation in fractionated montmorillonite nanoplatelet dispersions", *Colloid and Polymer Science*, 297(7), 1053-1065, 2019.
- [52] N. M. Kuznetsov, S. I. Belousov, A. V. Bakirov, S. N. Chvalun, R. A. Kamyshinsky, A. A. Mikhutkin, A. L. Vasiliev, P. M. Tolstoy, A. S. Mazur, E. D. Eidelman, E. B. Yudina, A. Y. Vul, "Unique rheological behavior of detonation nanodiamond hydrosols: The nature of sol-gel transition", *Carbon*, 161, 486-494, 2020.
- [53] Y. D. Liu, X. Quan, B. Hwang, Y. K. Kwon, H. J. Choi, "Core-shell-structured monodisperse copolymer/silica particle suspension and its electrorheological response", *Langmuir*, 30(7), 1729-1734, 2014.